

Article

Design of Molecular Water Oxidation Catalysts Stabilized by Ultrathin Inorganic Overlayers—Is Active Site Protection Necessary?

Laurent Sévery ¹, Sebastian Siol ² and S. David Tilley ^{1,*}

¹ Department of Chemistry, University of Zurich, Winterthurerstrasse 190, 8057 Zurich, Switzerland; laurent.severy@chem.uzh.ch

² EMPA, Uberlandstrasse 129, 8600 Dubendorf, Switzerland; sebastian.Siol@empa.ch

* Correspondence: david.tilley@chem.uzh.ch; Tel.: +41-44-635-46-75

Received: 4 September 2018; Accepted: 27 September 2018; Published: 29 September 2018



Abstract: Anchored molecular catalysts provide a good step towards bridging the gap between homogeneous and heterogeneous catalysis. However, applications in an aqueous environment pose a serious challenge to anchoring groups in terms of stability. Ultrathin overlayers embedding these catalysts on the surface using atomic layer deposition (ALD) are an elegant solution to tackle the anchoring group instability. The propensity of ALD precursors to react with water leads to the question whether molecules containing aqua ligands, such as most water oxidation complexes, can be protected without side reactions and deactivation during the deposition process. We synthesized two iridium and two ruthenium-based water oxidation catalysts, which contained an aqua ligand (Ir–OH₂ and Ru–OH₂) or a chloride (Ir–Cl and Ru–Cl) that served as a protecting group for the former. Using a ligand exchange reaction on the anchored and partially embedded Ru–Cl, the optimal overlayer thickness was determined to be 1.6 nm. An electrochemical test of the protected catalysts on meso-ITO showed different behaviors for the Ru and the Ir catalysts. The former showed no onset difference between protected and non-protected versions, but limited stability. Ir–Cl displayed excellent stability, whilst the unprotected catalyst Ir–OH₂ showed a later initial onset. Self-regeneration of the catalytic activity of Ir–OH₂ under operating conditions was observed. We propose chloride ligands as generally applicable protecting groups for catalysts that are to be stabilized on surfaces using ALD.

Keywords: atomic layer deposition; electrocatalysis; water splitting

1. Introduction

In recent years, research focusing on tackling the challenges of finite fossil fuel resources and renewable energies has greatly increased. One of the most promising approaches to tackle these challenges is storing solar energy in the form of chemical bonds to generate solar fuels [1]. Among several other technologies, photoelectrochemical (PEC) water splitting has been continuously gaining attention [2]. A PEC cell integrates both the light absorption by a photoabsorber and the catalysis in a single device. Over the last two decades, many new photoabsorber materials have emerged [3–6]. Furthermore, there has been significant improvement of the heterogeneous catalysts used to accelerate the water reduction (WRR) and the water oxidation reactions (WOR) [7,8]. These catalysts are usually made up of mixed transition metal compounds dispersed on the surface of the photoelectrode. Low overpotentials, high stability and scalable deposition of heterogeneous catalysts have made them attractive for commercial energy conversion applications [9,10].

In a parallel field of research, homogeneous catalysts for the WRR and WOR have been investigated. Molecular catalysts and transition-metal complexes, in particular, have been shown to

have excellent catalytic activities and benefit from high tunability by modification of the ligands [11–14]. Reaction mechanisms of homogeneous catalysts are more easily elucidated than heterogeneous ones, which helps to further improve their catalytic properties [15–18]. However, homogeneous approaches to water splitting suffer severe drawbacks. The WOR requires an energy source to drive the reaction, which must be provided either through chemical oxidants or through light. For the latter, the addition of a suitable photosensitizer and sacrificial electron acceptors is necessary. This leads to complicated mixtures required for the catalytic reaction, which become prone to side reactions and degradation of one or more components over time [19–21].

Therefore, combining the benefits of homogeneous catalysts with those of heterogenized ones is of great interest. Specifically, it was shown that several homogeneous WRR and WOR catalysts could be connected to electrode surfaces using specific binding groups on the extremities of the ligands [22]. This anchoring of transition-metal complexes has been successfully used in dye-sensitized solar cells, for which the most popular anchoring groups are carboxylic acids and phosphonates [23–26].

However, the stability of catalysts anchored to surfaces in the presence of water is limited, especially for carboxylic acids. Protection strategies of anchored complexes could resolve the problem, and have already been demonstrated to improve the lifetime of the bound species by several orders of magnitude [27,28]. Meyer et al. showed that by using atomic layer deposition (ALD), a technique used to deposit metal oxide layers with sub-nanometer resolution, molecular WOR catalysts anchored on metal oxide electrodes could be successfully stabilized [29,30].

The ALD process requires elevated temperatures and highly reactive precursors. Under those conditions, it is reasonable to assume that the process could lead to partial decomposition of molecular species on the electrode surfaces, leading to catalyst deactivation and degradation. Specifically, the organometallic ALD precursors are highly reactive towards certain functional groups, such as hydroxyls or amines [31,32]. For all water oxidation catalysts, a central requirement is the binding of a water molecule to the metal center, which is then oxidized by stepwise oxidation followed by release of oxygen. In this picture, the water oxidation complexes contain an aqua (OH_2) ligand bound to the central metal atom. As stated above, these aqua ligands are potential targets for side-reactions during the ALD process.

To assess the importance of these side reactions, we designed Ir and Ru based molecular water oxidation catalysts specifically for post-anchoring ALD protection using a chloride ligand as a protecting group, which under operating water splitting conditions undergoes ligand exchange with water to an active aqua complex (Figure 1). The design considers the necessary requirements for heterogenization of molecular catalysts, most importantly the single-site catalytic activity and the carboxylate anchoring groups. Furthermore, a nitrile group was incorporated in the Ru based catalysts as an infrared (IR) tag for characterization of the heterogenized catalyst. We compare the effect of ALD deposition on the chloride protected complexes with their unprotected aqua counterparts, using UV-Vis spectroscopy, IR-spectroscopy, X-ray photoelectron spectroscopy (XPS), and electrochemical techniques. We observe that the ALD-protected molecular species remains unchanged after catalysis, demonstrating the stabilizing effect of the ALD layer.

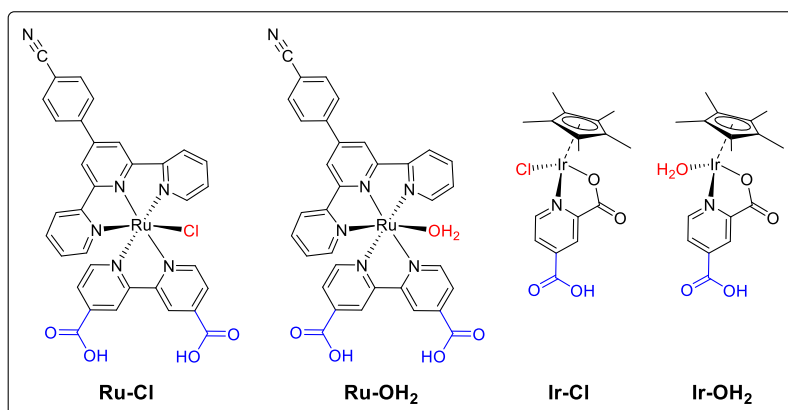


Figure 1. Molecular water oxidation (pre-)catalysts used in this work. The anchoring groups are shown in blue, the active site ligand (OH_2) or protecting group ligand (Cl) are shown in red.

2. Results and Discussion

The Ru-Cl complex was obtained in a simple two-step procedure by reacting RuCl_3 with the terpyridine (tpy) ligand, followed by the bipyridine dicarboxylic acid under reductive conditions, used for preparation of similar complexes, as described in Reference [33]. The Ir-Cl complex was synthesized according to a procedure described in Reference [34]. The aqua versions of the respective complexes were obtained by reacting the chloride precursor with a silver salt in the presence of water [33].

Mesoporous TiO_2 and ITO (meso- TiO_2 and meso-ITO) were determined to be suitable substrates for the investigation, as they are transparent and provide binding sites for carboxylic acids. Meso- TiO_2 was chosen for IR spectroscopic analysis of the complexes due to the transparency in the IR range (Figure S1), whereas meso-ITO was used for UV-Vis spectroscopy, electrochemical analyses, and XPS studies.

IR characterization was performed after anchoring of Ru-Cl and Ir-Cl onto meso- TiO_2 . As can be seen in Figure 2, the aromatic nitrile (CN_{Ar}) band on the tpy of Ru-Cl is present at 2230 cm^{-1} . As expected, for the Ir-Cl complex, no bands are observed in this region. After deposition of ALD- TiO_2 , the CN_{Ar} band of Ru-Cl is still present, although weaker than before, which could indicate a partial degradation of the nitrile group under ALD conditions (see Figures S2 and S3). Nevertheless, a significant amount of the complex was observed unaltered on the surface.

To verify whether the active site of the ALD-protected catalysts was still accessible, a ligand exchange reaction was used to replace the chloride ligand by a cyanide ligand. The anchored and protected complexes were submerged in a 1 M solution of sodium cyanide ($\text{pH} = 12$). Under these strongly basic conditions, desorption of unprotected molecular complexes is typically observed [35]. This allows for determination of active site accessibility at the same time as complex stability against desorption, which provides a practical tool for optimizing the thickness of the ALD- TiO_2 overlayer.

After immersion in the NaCN solution, the IR spectrum of the Ru-Cl complex showed two new peaks at 2082 cm^{-1} and around 2175 cm^{-1} . While the former can be attributed to the presence of a Ru-CN species [36], the broad band at 2175 cm^{-1} was shown to be due to adsorbed cyanide ions on TiO_2 , as a control experiment without anchored molecules led to a broad band in this region (Figure S4). The intensity of the CN_{Ar} band decreased, indicating partial desorption of the complex under the basic ligand exchange conditions. At lower ALD- TiO_2 thicknesses, complete loss of adsorbed Ru-Cl was observed, while at large overlayer thicknesses, complete burying of the anchored catalysts prevented the ligand exchange (Figure S4). These experiments led to an optimized layer thickness corresponding to 30 cycles of ALD- TiO_2 , which was measured to be 1.6 nm by ellipsometry on a reference piece of silicon wafer. In the case of the Ir-Cl complex, the previously optimized thickness of ALD- TiO_2 was used, and after ligand exchange, a band at 2113 cm^{-1} was observed, which was attributed to the

formation of an Ir–CN species [37]. From the ligand exchange experiments, we can conclude that the active site on the metal center of the chloride complexes does not undergo deactivation during the ALD protection of the molecules.

Using the optimized overlayer thickness, samples of all complexes on mesoporous ITO were prepared. UV-Vis analysis of the anchored catalysts before and after ALD deposition (Figures S5 and S6) show that the absorption maxima have a slight red-shift by 8 nm for Ru–Cl and Ru–OH₂, compared to the samples without TiO₂-overlayers. From the intensity of the absorption, no degradation of these molecules was evident (except for the CN_{Ar} group, from IR-spectroscopy). A lower coverage of Ru–Cl compared to Ru–OH₂ was observed. Unfortunately, the Ir complexes did not absorb strongly enough in the transmission range of ITO (400–800 nm) to allow for interpretation of their spectra.

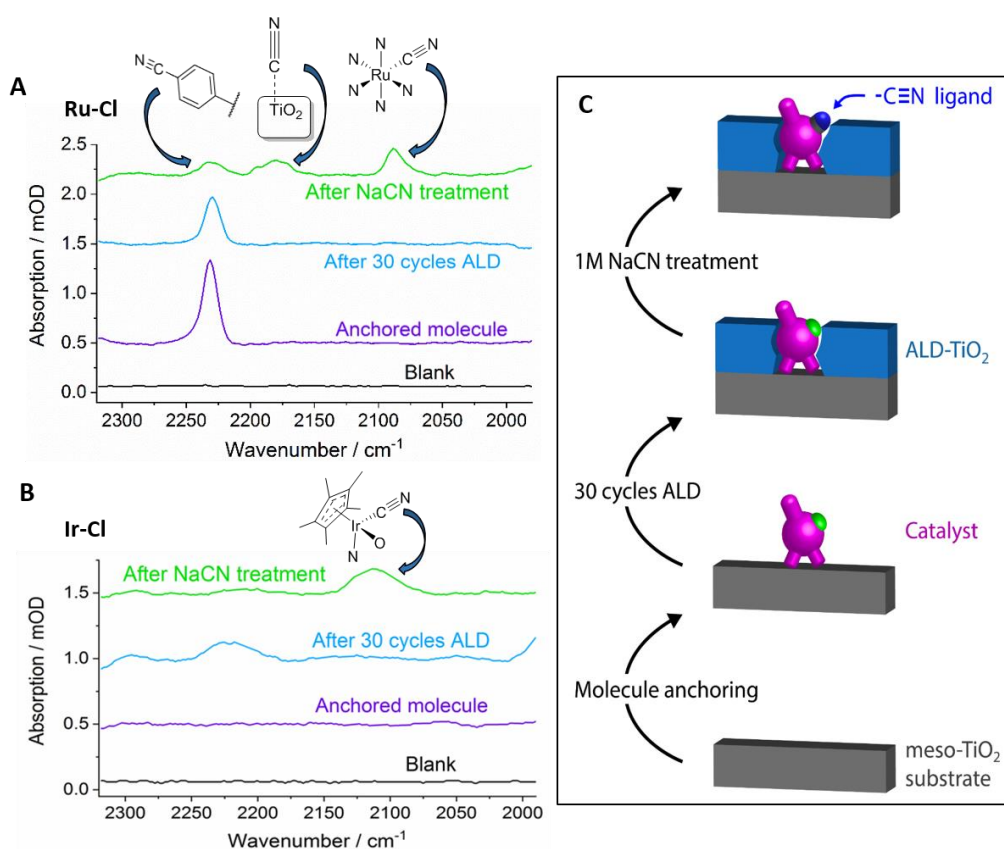


Figure 2. IR spectra of (A) Ru–Cl and (B) Ir–Cl adsorbed onto meso-TiO₂ after anchoring (purple), after ALD-TiO₂ deposition (blue) and after ligand exchange (green). (C) Schematic depiction of the process flow.

In the absence of an infrared handle on the Ir complex, we resorted to X-ray photoelectron spectroscopy (XPS) to characterize the heterogenized Ir catalyst. XPS analyses of the anchored Ir–Cl and Ir–OH₂ confirmed the presence of the complexes on the ITO coated substrates. XPS measurements were conducted before and after ALD. For samples with the ALD-TiO₂ overlayer, an overlap of the Ir 4f and Ti 3s core level regions, as well as low count rates of the Ir signal, rendered interpretation difficult. After deposition of 30 cycles ALD-TiO₂, the Ir 4f core level emission was almost completely attenuated. However, comparison with ALD-TiO₂ reference spectra revealed a weak contribution of the underlying Ir 4f molecule at approximately the same binding energy as observed before the ALD treatment (see Figure S7).

Using the optimized thickness of the ALD protective layer, catalyst molecules anchored on meso-ITO and encapsulated with 30 cycles ALD-TiO₂ were tested electrochemically to determine their activity for the WOR. The aqua and chloride versions of both the ruthenium and the iridium

based catalysts were compared in terms of their onset potential for water oxidation by performing 10 cycles of cyclic voltammetry (CV) in 0.1 M H_2SO_4 (Figure S8). Subsequently, the samples underwent chronoamperometry (CA) at 1.95 V vs. RHE for 30 min, followed by a post-electrolysis CV scan. This combination of an electrochemical test allows for stability and activity measurements of the surface-bound catalysts.

Figure 3 shows the third CV scan of the ALD-protected Ru and Ir catalysts. The Ru-Cl and Ru-OH₂ samples display a reversible oxidation peak around 1.25 V, which is in good agreement with literature values [33,38]. The catalytic onset for water oxidation begins at ca. 1.7 V for both Ru-OH₂ and Ru-Cl; however, due to lower loading of the Ru-Cl sample, the catalytic current obtained is lower. Both Ru catalysts showed decreasing current in subsequent CV scans, indicating desorption under strong oxidative bias despite the ALD protection layer. This observation was further underlined by a steady decrease of current down to the low microampere range during CA (Figure S9). After 30 min at 1.95 V, CV of the Ru catalysts no longer showed redox peaks and only a small increase of current was observed at the WOR onset.

The similarity of the CV scans of Ru-Cl and Ru-OH₂ led to the conclusion that the active catalyst was the same, the ruthenium aqua complex, which showed that the chloride ligand could indeed be exchanged for aqua under operating conditions. However, the lack of a difference in onset potential for the Ru-OH₂ complex indicated that the aqua ligand is not (completely) blocked or deactivated during the ALD process, making the requirement of a protecting group unnecessary in this case. Under the preparation conditions (soaking of the meso-ITO in MeOH solutions of catalyst), it is possible that the aqua ligand may be partially displaced by a methoxy ligand, which would form an in situ protecting group. This might explain why other authors observed no deactivation of ruthenium aqua based catalysts during ALD-protection [29].

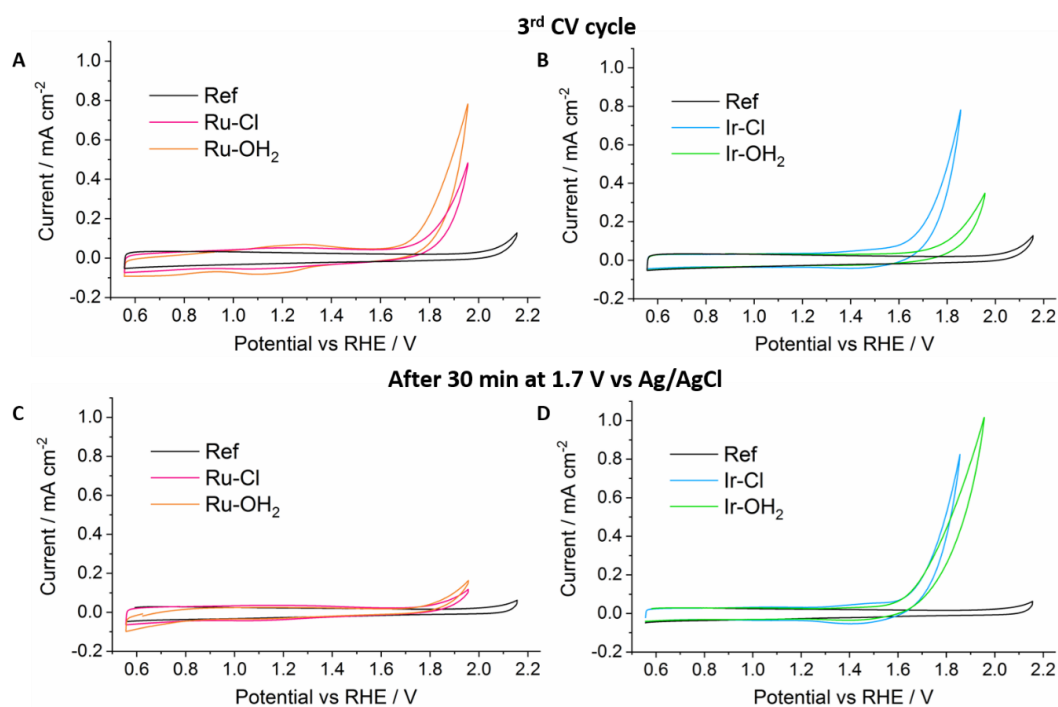


Figure 3. Top: Cyclic voltammetry (CV) scans of Ru-Cl (pink), Ru-OH₂ (orange) (A), Ir-Cl (blue) and Ir-OH₂ (green) (B) before chronoamperometry at 1.95 V vs. RHE. Bottom: CV scans of Ru-Cl (pink), Ru-OH₂ (orange) (C), Ir-Cl (blue) and Ir-OH₂ (green) (D) after chronoamperometry. CVs were recorded at 50 mV/s in 0.1 M H_2SO_4 with a Pt counter electrode. Ref is meso-ITO with 30 cycles ALD-TiO₂.

The Ir complexes showed a different behavior. In the CV scans before CA, there was a clear onset difference of around 200 mV between Ir–Cl and Ir–OH₂, with the former beginning to catalyze water oxidation at 1.6 V vs. Ag/AgCl (380 mV overpotential vs. the thermodynamic water oxidation potential). The CV curve of Ir–OH₂ also showed a less steep rise at higher potential, indicating a larger resistance. We attribute this to the formation of a deactivated molecular iridium species, which is significantly hindered to catalyze water oxidation. A reasonable mechanism that illustrates the different behavior of Ir–Cl and Ir–OH₂ is shown in Figure 4. The chloride complex remains unaffected by the ALD layer growth, whilst the aqua complex undergoes a reaction between the titanium precursor tetrakis(dimethylamido)titanium (TDMAT) and the aqua ligand.

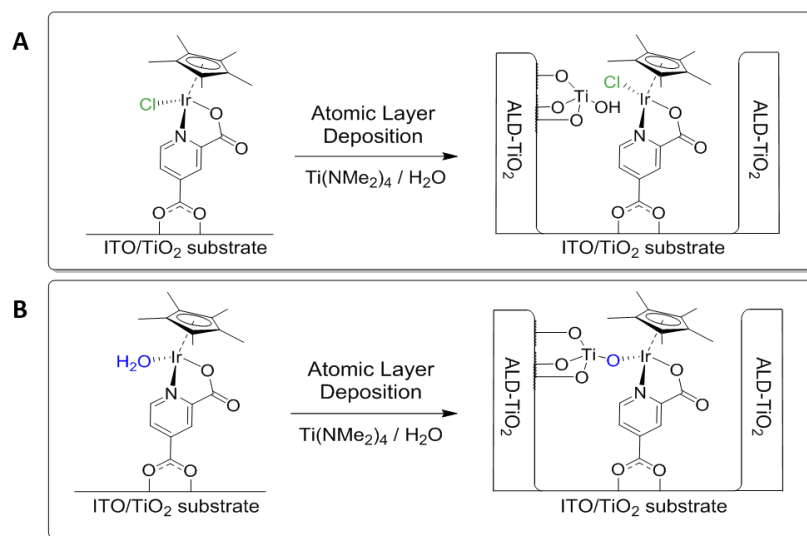


Figure 4. Reaction of anchored molecular Ir–Cl (A) and Ir–OH₂ (B) during the deposition of ALD-TiO₂ using TDMAT/water as precursors. Ir–Cl remains unchanged during ALD and is encapsulated in a TiO₂ layer, while Ir–OH₂ undergoes a reaction between the aqua ligand and the TDMAT, leading to a deactivated Ir complex embedded in TiO₂.

During CA of the Ir complexes, we observed that the current of the Ir–OH₂ sample increased towards that of the Ir–Cl. Both showed only relatively small long-term losses of current during the 30 min CA measurement, indicating good stability of the bound complexes in this time range. Indeed, the subsequent CV scan clearly showed that there was no loss of activity for Ir–Cl, and that the Ir–OH₂ complex had in fact approached Ir–Cl in terms of WOR activity.

To explain this, we propose a self-regeneration of the Ir–OH₂ complex that was deactivated during deposition of ALD-TiO₂. Under operating conditions in strong acid, the deactivated Ir species could hydrolyze to form the active Ir–OH₂ and a titanol unit (Figure 5A). However, previous research suggests that oxidative decomposition of the Cp* ligand is necessary to form a catalytically active species [39–43]. An alternative activation pathway that proceeds via ligand oxidation under operating conditions is shown in Figure 5B. The chloride ligand does not react with the ALD precursor and can therefore be converted into the active aqua form directly under operation, without requiring any activation. The active catalyst may then perform water oxidation without previously oxidizing the Cp* ligand. In this picture, the chloride acts as an exchangeable protecting group for the Ir catalyst. Remarkably, the Ir-based ALD-protected catalysts remained active over 30 min under strong bias, without desorbing. This clearly shows the benefits that ALD overlayers can bring for stabilization of carboxylic acid-anchored molecular catalysts on electrode surfaces.

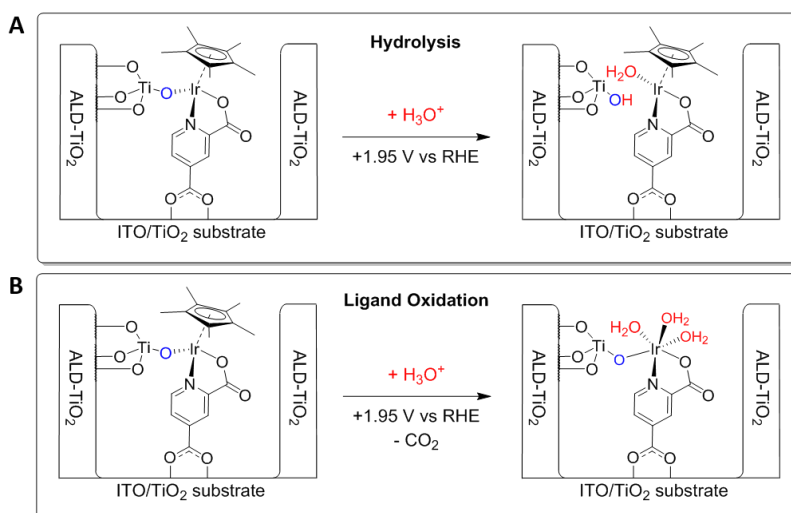


Figure 5. Proposed hydrolytic (A) and Cp* ligand oxidation (B) mechanisms for (re)generation of the active Ir-OH₂ catalyst under operating conditions, which had undergone deactivation during the deposition of the ALD-TiO₂ layer.

To assess the stability of the Ir-based catalysts, XPS was measured on the anchored and ALD-protected samples before and after the electrochemical measurement (Figure 6). The difference spectra showed that there was no measurable change in the combined Ir 4f and Ti 3s core level emission after 30 min under operation, indicating the stability of Ir-Cl and Ir-OH₂ after ALD-protection. One would expect a significant change in the Ir 4f binding energy upon oxidative degradation of the Cp* ligand, which was not observed. However, due to the rather weak Ir signal, we cannot conclusively determine which of the pathways in Figure 5 is operative.

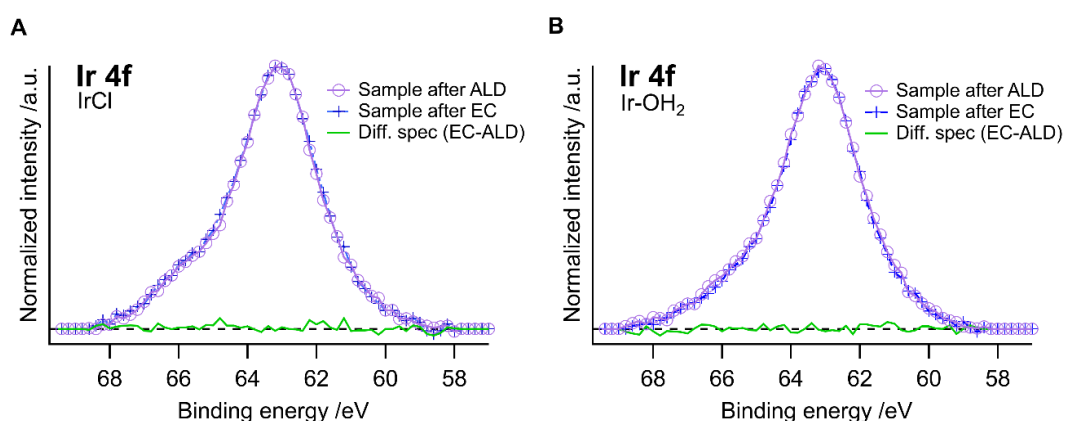


Figure 6. XPS spectra of (A) Ir-Cl and (B) Ir-OH₂ with ALD-TiO₂ before and after electrochemical measurements. The respective difference spectra are shown in green.

3. Materials and Methods

3.1. General

Unless stated otherwise, all reactions were carried out under a nitrogen atmosphere. All chemicals and solvents were used as purchased without further purification. ¹H and ¹³C spectra were recorded using a Bruker 400 or 500 MHz spectrometer. The signals were referenced to residual solvent signals. Chemical shifts were reported in ppm. IR spectra of molecules were recorded on a Bruker IR spectrometer. UV-Vis spectra were recorded on a Shimadzu UV-3600 spectrometer using a quartz cell (L = 1 cm). Electrochemical experiments were carried out on a Biologic SP-50 potentiostat.

High-resolution mass spectra were acquired on a QExactive instrument (ThermoFisher Scientific, Bremen, Germany) equipped with a heated electrospray (ESI) ionization source and connected to a Dionex Ultimate 3000 UHPLC system (ThermoFischer Scientifics, Germering, Germany). The samples were dissolved in MeOH, a positive detection mode was used.

[Cp*Ir(κ -N,O-lutidine)Cl] (Ir-Cl) was synthesized according to a published procedure in Reference [34].

3.2. Materials

3.2.1. 4'-(4-Cyanophenyl)-2,2':6',2''-terpyridine (tpy-PhCN)

The ligand was synthesized using a Kröhnke-type reaction approach, as described in Reference [44]. 4-Cyanobenzaldehyde (1.994 g, 15.2 mmol, 1 eq) was dissolved in 80 mL MeOH, then KOH (0.91 g, 16 mmol, 1.05 eq) and concentrated NH₄OH (25%, 15 mL) were added to the solution. Next, 2-acetylpyridine (3.42 mL, 30.5 mmol, 1 eq) was added, and the solution was heated to reflux for 2.5 h. A white precipitate formed and was filtered off after cooling the reaction mixture to room temperature. The precipitate was washed with cold MeOH (80 mL) and ether (20 mL), then air dried. Yield: 1.74 g, 34%. Analysis (conforms to Reference [45]): ¹H NMR (400 MHz, Chloroform-*d*): 8.78–8.71 (m, 4H), 8.69 (d, 2H), 8.00 (d, 2H), 7.91 (dd, 2H), 7.81 (d, 2H), 7.38 (dd, 2H).

3.2.2. Synthesis of [Ru(tpy-PhCN)Cl₃]

4'-(4-cyanophenyl)-2,2':6',2''-terpyridine (0.134 g, 0.4 mmol, 1 eq) and RuCl₃ × H₂O (0.098 g, 0.4 mmol, 1 eq) were refluxed in methanol for 4 h under nitrogen. The resulting red–brown powder was filtered off and washed with cold methanol and diethyl ether. The product was dried at 50 °C for 10 min, yielding a brown powder (0.185 g). The product was used without further purification. IR (cm⁻¹): 2227, 1598, 1531, 1468, 1425, 1399, 1289, 1245.

3.2.3. Synthesis of [Ru(tpy-PhCN)(bda)Cl]Cl (Ru-Cl)

[Ru(tpy-PhCN)Cl₃] (0.055 g) and 2,2'-bipyridine-4,4'-dicarboxylic acid (0.025 g) were suspended in a water-ethanol mixture (1:3, 12 mL). After degassing by bubbling with N₂ for 10 min, trimethylamine (0.1 mL) was added and the reaction mixture was refluxed for 4.5 h. After cooling, the reaction was filtered and the filtrate washed with methanol (10 mL). The filtrate solution was basified with KOH/KCl in water (1 M each), washed with MeOH/THF/CHCl₃ 2:1:3 and then acidified with conc. HCl. The aqueous phase was extracted twice with the organic solvent mixture, the organic phase then dried over MgSO₄, and concentrated in vacuo. The crude product was dissolved in MeOH, filtered through a pad of celite, and finally concentrated to dryness. Yield: 0.020 g, 27%. ¹H NMR (400 MHz, Methanol-*d*₄) δ 10.40 (d, *J* = 5.9 Hz, 1H), 9.27 (s, 1H), 9.05 (s, 2H), 8.97 (s, 1H), 8.74 (d, *J* = 7.9 Hz, 2H), 8.50 (d, *J* = 5.8 Hz, 1H), 8.36 (d, *J* = 8.5 Hz, 2H), 8.05 (d, *J* = 8.5 Hz, 2H), 7.99 (dd, *J* = 7.9 Hz, 2H), 7.74 (d, *J* = 5.9 Hz, 1H), 7.70 (d, *J* = 5.3 Hz, 2H), 7.54 (d, *J* = 4.2 Hz, 1H), 7.36 (dd, 2H). ¹³C NMR (126 MHz, Methanol-*d*₄) δ 165.31, 164.60, 159.51, 158.50, 157.98, 156.76, 153.07, 152.48, 152.19, 145.69, 141.40, 138.34, 137.50, 137.28, 132.94, 128.32, 127.40, 125.94, 125.19, 123.98, 123.05, 122.56, 120.60, 117.89, 113.21. HRMS: [M]⁺ 715.04301 (calc. 715.04291). IR (cm⁻¹): 2224, 1702, 1637, 1605, 1551, 1470, 1432, 1402, 1383, 1309, 1290, 1248, 1227.

3.2.4. Synthesis of [Ru(tpy-PhCN)(bda)(OH₂)](ClO₄)₂ (Ru-OH₂)

A solution of AgClO₄ in deionized water (8.5 mg in 3.2 mL, 2.1 equiv) was added to a Schlenk flask containing [Ru(tpy-PhCN)(bda)Cl]Cl (14.8 mg, 1 eq), and the solution was refluxed for 2 h under N₂. After cooling, the reaction mixture was filtered through celite using water as eluent. The product was obtained after drying in a stream of nitrogen as a red–black microcrystalline solid. ¹H NMR (500 MHz, DMSO-*d*₆) δ 9.98 (d, *J* = 5.7 Hz, 1H), 9.39 (s, 2H), 9.03 (d, *J* = 8.2 Hz, 2H), 8.95 (s, 1H), 8.72 (s, 1H), 8.57 (d, *J* = 8.4 Hz, 2H), 8.31 (d, *J* = 5.9 Hz, 1H), 8.27 (d, *J* = 8.3 Hz, 2H), 8.23 (t, *J* = 7.8 Hz, 2H),

7.85 (d, $J = 5.2$ Hz, 2H), 7.58–7.51 (m, 3H), 7.23 (d, $J = 5.7$ Hz, 1H). HRMS: $[M - H_2O + CH_3OH]^+$ 711.09239 (calc. 711.09244).

3.2.5. Synthesis of $[Cp^*Ir(\kappa-N,O\text{-lutidine})(OH_2)](ClO_4)$ (Ir–OH₂)

$[Cp^*Ir(\kappa-N,O\text{-lutidine})Cl]$ (55.2 mg, 1 equiv) was added to a solution of $AgClO_4$ (22.8 mg, 1.05 equiv.) in MeCN/ H_2O 5:1 (6 mL) and stirred for 30 min, during which a white precipitate formed. The reaction solution was filtered through celite, washed with 1 mL MeCN, and the solvent removed under reduced pressure, yielding a green-yellow powder. Yield: 51 mg, 80%. 1H NMR (500 MHz, Acetone- d_6) δ 9.12 (d, $J = 5.6$ Hz, 1H), 8.42 (d, $J = 1.4$ Hz, 1H), 8.25 (dd, $J = 5.7, 1.9$ Hz, 1H), 1.74 (s, 15H). ^{13}C NMR (126 MHz, Acetone) δ 163.90*, 151.84, 140.71*, 128.75, 126.22, 86.15, 8.08 (signals denoted with * from HMBC experiment; 2 quaternary carbons could not be measured). HRMS: $[M - H_2O]^+$ 494.09411 (calc. 494.09378).

3.2.6. Preparation of ITO Spin Coating Solution

ITO particles (18 nm, 99.99%, US Research Nanomaterials Inc., Houston, TX, USA) (2 g) were sonicated in ethanol for 20 min. A solution of ethyl cellulose (0.2 g), alcohol surfactant (proprietary nanopowder dispersant, US Research Nanomaterials Inc.) (0.225 g), and terpineol (5 g) in ethanol (5 mL) was added to the ITO suspension. The volatiles of the resulting mixture were removed by rotary evaporation (30 min) to form a viscous blue paste. The spin coating solution was made by diluting the obtained paste with ethanol in a 1:4 ratio.

3.2.7. Preparation of TiO_2 Spin Coating Solution

50 nm rutile particles (50 nm, 99.9%, rutile, US Research Nanomaterials Inc.) (2 g) and a solution of ethanol, acetic acid, and water (5:5:1 by volume) (5 mL) were ball-milled with 0.2 mm zirconia balls for 3 h at 500 rpm. After sieving off the zirconia balls, the particles were suspended in ethanol. To this suspension was added a solution of ethyl cellulose (0.5 g) and terpineol (5 g) in ethanol (25 mL). The ethanol was then removed from the resulting mixture by rotary evaporation. Then, 50 mL of ethanol were added, the mixture sonicated for 30 min, and the volatiles again removed. The spin coating solution was made by diluting the viscous white paste with 36 mL of ethanol.

3.2.8. Preparation of Mesoporous Substrates

An FTO on glass window (FTO TEC 15, Pilkington, Tokyo, Japan) was cut into pieces (1.25 × 2.5 cm for TiO_2 , 1 × 2.5 cm for ITO) and cleaned by sonicating in acetone, Deconex solution in water (5%), distilled water, and ethanol for 10 min each. After drying in a stream of N_2 , the pieces were partially covered with Kapton tape on the conductive face, leaving a free area of 1.5 cm². Freshly sonicated spin coating solutions were first applied to the samples, which were then spun at 2000 rpm for 20 s, using an acceleration of 500 rpm per second. After spin coating, the samples were dried on a hot plate at 125 °C for 5 min. The spin coating and drying process was repeated 3 times. After the final spin coating, the Kapton tape was removed and the samples sintered in air at 550 °C for one hour (TiO_2), or 450 °C for 30 min (ITO).

3.2.9. Anchoring of Molecular Catalysts on Substrates

Molecules were anchored on the mesoporous substrates by submersion in a 0.2 mM methanolic solution for one hour or overnight. After catalyst anchoring, the substrates were placed in pure methanol (10 mL) for 30 min before being dried under N_2 .

3.2.10. Atomic Layer Deposition

ALD deposition of TiO_2 was performed using a Picosun R200 deposition system, using tetrakis-(dimethylamido)titanium(IV) (99.999%, Sigma-Aldrich, Buchs, Switzerland) and Milli-Q water

as precursors, and N₂ (99.9999%) as carrier gas. The titanium precursor was kept at 85 °C throughout the deposition process, whilst the water was kept at 25 °C. The substrate and reactor were kept at 120 °C during the deposition. A protocol for high surface area substrates was used to deposit the TiO₂ layers on the mesoporous substrates. Each cycle consisted of an initial 2 s TDMAT pulse, followed by a 20 s purge. A water pulse of 0.1 s followed by a 20 s purge was then applied. A flow rate of 30 sccm for both TDMAT and water was used for this process. Growth of the layers was tracked by inserting a 1 × 1 cm piece of silicon wafer into the reactor and measuring the resulting film thickness by ellipsometry. An average growth rate of 0.054 nm/cycle was observed.

3.3. Methods

3.3.1. Ligand Exchange Experiments and IR Spectroscopy

FTIR spectra were measured in external reflection using the mesoporous substrates described above: As-prepared, before and after anchoring of the molecules, and after ALD. The samples were then submerged in a freshly prepared 1 M solution of NaCN for 30 min. They were then rinsed by repeated dipping in distilled water, then soaked in EtOH for 2 min. The samples were finally dried under N₂ flow. Spectra were acquired after the ligand exchange. For the analysis of the CN stretching bands, a baseline correction using a polynomial fit in the region between 2300 cm⁻¹ and 2000 cm⁻¹ was applied.

3.3.2. Electrochemical Analyses

Unless otherwise noted, cyclic voltammetry and chronoamperometry were performed in 0.1 M sulfuric acid solution (pH = 1), with an Ag/AgCl (saturated KCl) reference electrode and a platinum wire as a counter electrode. The scan rate was 50 mV/s. The substrates were connected from the bare FTO part and submerged to completely cover the mesoporous layer. Current densities were normalized to geometric areas of the mesoporous layers of the samples. Voltages were reported vs. the reversible hydrogen electrode (RHE) by converting the potentials measured with the Ag/AgCl electrode using the Nernst equation, according to the following formula:

$$E_{\text{RHE}} = E_{\text{Ag/AgCl}} + 0.059 \cdot \text{pH} + E_{\text{Ag/AgCl}}^0 \quad (1)$$

3.3.3. X-ray Photoelectron Spectroscopy (XPS)

XPS was conducted on selected samples using a Physical Electronics (PHI) Quantum 2000 X-ray photoelectron spectrometer (Physical Electronics, Ismaning, Germany) featuring monochromatic Al-K α radiation, generated from an electron beam operated at 15 kV and 32.3 W. The energy scale of the instrument was calibrated using Au and Cu reference samples. The samples were firmly pressed onto indium foil patches, which were then mounted onto a sample platen and introduced into the spectrometer. The analysis was conducted at 8 E-9 mbar, with an electron take off angle of 45° and a pass energy of 46.95 eV for all samples. Owing to the low count rate of the Ir 4f core level emission, measurement times in excess of 8 h per sample were used. Measurements were repeated using different exposure times to ensure no X-ray beam damage occurred on the specimen. Ir 4f core level emissions were fitted for a qualitative comparison between different samples using Voigt profiles (GL30), with a double separation of 2.9 eV for each individual component. The line shape of the Ti 3s emission, which was used for the interpretation of the combined Ti 3s and Ir 4f spectra, was fitted on a reference ALD-TiO₂ sample processed under identical conditions.

4. Conclusions

Ruthenium and iridium based water oxidation catalysts with carboxylate anchoring groups have successfully been synthesized and grafted onto meso-TiO₂ and meso-ITO substrates. ALD-TiO₂ was deposited to prevent the anchored catalysts from desorbing. We showed that the ALD protection

reduces and prevents desorption in strongly acidic aqueous environments. The Ru catalysts could not be stabilized under strongly oxidizing operating conditions for prolonged times. In contrast, the Ir catalysts showed no degradation, even under strong oxidative bias. When comparing the aqua and chloride version of the complexes, we observed different behavior during the deposition of the ALD-TiO₂ layer. While the Ru complexes seemed to remain unaffected by the presence of TDMAT during the protection layer growth, Ir-OH₂ showed catalytic deactivation compared to Ir-Cl, presumably due to a reaction between the aqua ligand and TDMAT. Under operating conditions, the deactivated Ir catalysts were regenerated.

Chloride ligands as protecting groups for water oxidation catalysts are a viable strategy to prevent deactivation and degradation during ALD deposition of protecting layers. Chloride-protected active sites are much less prone to undesired reactions with ALD precursors. We note that in some cases, protection is not necessary (Ru catalysts). Furthermore, self-regeneration of deactivated catalysts may take place and make protecting groups redundant. As this regeneration process is not a given for all deactivated catalyst systems, using chloride ligand as a protecting group is a simple way to ensure an active catalyst after ALD protection.

Supplementary Materials: The following are available online at <http://www.mdpi.com/2304-6740/6/4/105/s1>, Figure S1: IR spectrum of meso-TiO₂ support, Figure S2: Raw IR spectra of Ru-Cl with increasing ALD layer thickness, Figure S3: Ru-Cl IR spectra after baseline correction in the relevant range, Figure S4: IR spectra of Ru-Cl after NaCN treatment, with varying ALD-layer thickness, Figure S5: UV-Vis spectra before ALD, Figure S6: UV-Vis spectra after ALD, Figure S7: XPS spectra before and after ALD deposition, Figure S8: Full CV scans, Figure S9: Chronoamperometric data.

Author Contributions: L.S. and S.D.T. conceived the project. L.S. carried out all of the experiments. S.S. carried out the XPS measurements and prepared the XPS figures. L.S. wrote the paper with feedback from S.S. and S.D.T.

Funding: This research was funded by the Swiss National Science Foundation, AP Energy Grant # PYAPP2 160586, and the University of Zurich Research Priority Program (URPP) LightChEC. Sebastian Siol acknowledges funding from the COST project IZCNZ0-174856 C16.0075, in the COST Action MP1407 (e-MINDS).

Acknowledgments: We thank Philip Kraack and the group of Peter Hamm (UZH) for guidance during the IR measurements and for the use of their IR instrumentation.

Conflicts of Interest: The authors declare no conflict of interest.

References

1. Walter, M.G.; Warren, E.L.; McKone, J.R.; Boettcher, S.W.; Mi, Q.; Santori, E.A.; Lewis, N.S. Solar water splitting cells. *Chem. Rev.* **2010**, *110*, 6446–6473. [[CrossRef](#)] [[PubMed](#)]
2. Jiang, C.; Moniz, S.J.A.; Wang, A.; Zhang, T.; Tang, J. Photoelectrochemical devices for solar water splitting—Materials and challenges. *Chem. Soc. Rev.* **2017**, *46*, 4645–4660. [[CrossRef](#)] [[PubMed](#)]
3. Prabhakar, R.R.; Septina, W.; Siol, S.; Moehl, T.; Wick-Joliat, R.; Tilley, S.D. Photocorrosion-resistant Sb₂Se₃ photocathodes with earth abundant MoS_x hydrogen evolution catalyst. *J. Mater. Chem. A* **2017**, *5*, 23139–23145. [[CrossRef](#)]
4. Wick, R.; Tilley, S.D. Photovoltaic and Photoelectrochemical Solar Energy Conversion with Cu₂O. *J. Phys. Chem. C* **2015**, *119*, 26243–26257. [[CrossRef](#)]
5. Abdi, F.F.; Han, L.; Smets, A.H.M.; Zeman, M.; Dam, B.; Van De Krol, R. Efficient solar water splitting by enhanced charge separation in a bismuth vanadate-silicon tandem photoelectrode. *Nat. Commun.* **2013**, *4*, 1–7. [[CrossRef](#)] [[PubMed](#)]
6. Zhu, X.; Guijarro, N.; Liu, Y.; Schouwink, P.; Wells, R.A.; Le Formal, F.; Sun, S.; Gao, C.; Sivula, K. Spinel Structural Disorder Influences Solar-Water-Splitting Performance of ZnFe₂O₄ Nanorod Photoanodes. *Adv. Mater.* **2018**, 1801612. [[CrossRef](#)] [[PubMed](#)]
7. Roger, I.; Shipman, M.A.; Symes, M.D. Earth-abundant catalysts for electrochemical and photoelectrochemical water splitting. *Nat. Rev. Chem.* **2017**, *1*. [[CrossRef](#)]
8. Hou, Y.; Zhuang, X.; Feng, X. Recent Advances in Earth-Abundant Heterogeneous Electrocatalysts for Photoelectrochemical Water Splitting. *Small Methods* **2017**, *1*, 1700090. [[CrossRef](#)]

9. Benck, J.D.; Chen, Z.; Kuritzky, L.Y.; Forman, A.J.; Jaramillo, T.F. Amorphous molybdenum sulfide catalysts for electrochemical hydrogen production: Insights into the origin of their catalytic activity. *ACS Catal.* **2012**, *2*, 1916–1923. [[CrossRef](#)]
10. Qian, M.; Cui, S.; Jiang, D.; Zhang, L.; Du, P. Highly Efficient and Stable Water-Oxidation Electrocatalysis with a Very Low Overpotential using FeNiP Substitutional-Solid-Solution Nanoplate Arrays. *Adv. Mater.* **2017**, *29*. [[CrossRef](#)] [[PubMed](#)]
11. Joliat, E.; Schnidrig, S.; Probst, B.; Bachmann, C.; Spingler, B.; Baldrige, K.K.; Von Rohr, F.; Schilling, A.; Alberto, R. Cobalt complexes of tetradentate, bipyridine-based macrocycles: Their structures, properties and photocatalytic proton reduction. *Dalton Trans.* **2016**, *45*, 1737–1745. [[CrossRef](#)] [[PubMed](#)]
12. Matheu, R.; Ertem, M.Z.; Benet-Buchholz, J.; Coronado, E.; Batista, V.S.; Sala, X.; Llobet, A. Intramolecular Proton Transfer Boosts Water Oxidation Catalyzed by a Ru Complex. *J. Am. Chem. Soc.* **2015**, *137*, 10786–10795. [[CrossRef](#)] [[PubMed](#)]
13. Wilson, A.D.; Newell, R.H.; McNevin, M.J.; Muckerman, J.T.; DuBois, M.R.; DuBois, D.L. Hydrogen oxidation and production using nickel-based molecular catalysts with positioned proton relays. *J. Am. Chem. Soc.* **2006**, *128*, 358–366. [[CrossRef](#)] [[PubMed](#)]
14. Kilgore, U.J.; Roberts, J.A.S.; Pool, D.H.; Appel, A.M.; Stewart, M.P.; DuBois, M.R.; Dougherty, W.G.; Kassel, W.S.; Bullock, R.M.; DuBois, D.L. $[\text{Ni}(\text{P}^{\text{Ph}}_2 \text{N}^{\text{C}_6\text{H}_4\text{X}_2})_2]^{2+}$ Complexes as Electrocatalysts for H_2 Production: Effect of Substituents, Acids, and Water on Catalytic Rates. *J. Am. Chem. Soc.* **2011**, *133*, 5861–5872. [[CrossRef](#)] [[PubMed](#)]
15. Junge, H.; Marquet, N.; Kammer, A.; Denurra, S.; Bauer, M.; Wohlrab, S.; Gärtner, F.; Pohl, M.M.; Spannenberg, A.; Gladiali, S.; et al. Water oxidation with molecularly defined iridium complexes: Insights into homogeneous versus heterogeneous catalysis. *Chem. Eur. J.* **2012**, *18*, 12749–12758. [[CrossRef](#)] [[PubMed](#)]
16. Abbott, D.F.; Lebedev, D.; Waltar, K.; Povia, M.; Nachtegaal, M.; Fabbri, E.; Copéret, C.; Schmidt, T.J. Iridium Oxide for the Oxygen Evolution Reaction: Correlation between Particle Size, Morphology, and the Surface Hydroxo Layer from Operando XAS. *Chem. Mater.* **2016**, *28*, 6591–6604. [[CrossRef](#)]
17. Codolà, Z.; Cardoso, J.M.S.; Royo, B.; Costas, M.; Lloret-Fillol, J. Highly Effective Water Oxidation Catalysis with Iridium Complexes through the Use of NaIO_4 . *Chem. Eur. J.* **2013**, *19*, 7203–7213. [[CrossRef](#)] [[PubMed](#)]
18. Liu, X.; Maegawa, Y.; Goto, Y.; Hara, K.; Inagaki, S. Heterogeneous Catalysis for Water Oxidation by an Iridium Complex Immobilized on Bipyridine-Periodic Mesoporous Organosilica. *Angew. Chem Int. Ed.* **2016**, *55*, 7943–7947. [[CrossRef](#)] [[PubMed](#)]
19. Rodenberg, A.; Oraziotti, M.; Mosberger, M.; Bachmann, C.; Probst, B.; Alberto, R.; Hamm, P. Quinones as Reversible Electron Relays in Artificial Photosynthesis. *ChemPhysChem* **2016**, *17*, 1321–1328. [[CrossRef](#)] [[PubMed](#)]
20. Windisch, J.; Oraziotti, M.; Hamm, P.; Alberto, R.; Probst, B. General Scheme for Oxidative Quenching of a Copper Bis-Phenanthroline Photosensitizer for Light-Driven Hydrogen Production. *ChemSusChem* **2016**, *9*, 1719–1726. [[CrossRef](#)] [[PubMed](#)]
21. Li, J.; Güttinger, R.; Moré, R.; Song, F.; Wan, W.; Patzke, G.R. Frontiers of water oxidation: the quest for true catalysts. *Chem. Soc. Rev.* **2017**, *46*, 6124–6147. [[CrossRef](#)] [[PubMed](#)]
22. Odrobina, J.; Scholz, J.; Pannwitz, A.; Francàs, L.; Dechert, S.; Llobet, A.; Jooss, C.; Meyer, F. Backbone Immobilization of the Bis(bipyridyl)pyrazolate Diruthenium Catalyst for Electrochemical Water Oxidation. *ACS Catal.* **2017**, *7*, 2116–2125. [[CrossRef](#)]
23. Zhang, L.; Cole, J.M. Anchoring Groups for Dye-Sensitized Solar Cells. *ACS Appl. Mater. Interfaces* **2015**, *7*, 3427–3455. [[CrossRef](#)] [[PubMed](#)]
24. Galoppini, E. Linkers for anchoring sensitizers to semiconductor nanoparticles. *Coord. Chem. Rev.* **2004**, *248*, 1283–1297. [[CrossRef](#)]
25. Boissezon, R.; Muller, J.; Beaugeard, V.; Monge, S.; Robin, J.-J. Organophosphonates as anchoring agents onto metal oxide-based materials: synthesis and applications. *RSC Adv.* **2014**, *4*, 35690. [[CrossRef](#)]
26. Materna, K.L.; Rudshhteyn, B.; Brennan, B.J.; Kane, M.H.; Bloomfield, A.J.; Huang, D.L.; Shopov, D.Y.; Batista, V.S.; Crabtree, R.H.; Brudvig, G.W. Heterogenized Iridium Water-Oxidation Catalyst from a Silatrane Precursor. *ACS Catal.* **2016**, *6*, 5371–5377. [[CrossRef](#)]
27. Lauinger, S.M.; Piercy, B.D.; Li, W.; Yin, Q.; Collins-Wildman, D.L.; Glass, E.N.; Losego, M.D.; Wang, D.; Geletii, Y.V.; Hill, C.L. Stabilization of Polyoxometalate Water Oxidation Catalysts on Hematite by Atomic Layer Deposition. *ACS Appl. Mater. Interfaces* **2017**, *9*, 35048–35056. [[CrossRef](#)] [[PubMed](#)]

28. Son, H.J.; Prasittichai, C.; Mondloch, J.E.; Luo, L.; Wu, J.; Kim, D.W.; Farha, O.K.; Hupp, J.T. Dye stabilization and enhanced photoelectrode wettability in water-based dye-sensitized solar cells through post-assembly atomic layer deposition of TiO₂. *J. Am. Chem. Soc.* **2013**, *135*, 11529–11532. [[CrossRef](#)] [[PubMed](#)]
29. Vannucci, A.K.; Alibabaei, L.; Losego, M.D.; Concepcion, J.J.; Kalanyan, B.; Parsons, G.N.; Meyer, T.J. Crossing the divide between homogeneous and heterogeneous catalysis in water oxidation. *Proc. Natl. Acad. Sci. USA* **2013**, *110*, 20918–20922. [[CrossRef](#)] [[PubMed](#)]
30. Hanson, K.; Losego, M.D.; Kalanyan, B.; Parsons, G.N.; Meyer, T.J. Stabilizing small molecules on metal oxide surfaces using atomic layer deposition. *Nano Lett.* **2013**, *13*, 4802–4809. [[CrossRef](#)] [[PubMed](#)]
31. Xie, Q.; Jiang, Y.-L.; Detavernier, C.; Deduytsche, D.; Van Meirhaeghe, R.L.; Ru, G.-P.; Li, B.-Z.; Qu, X.-P. Atomic layer deposition of TiO₂ from tetrakis-dimethyl-amido titanium or Ti isopropoxide precursors and H₂O. *J. Appl. Phys.* **2007**, *102*, 083521. [[CrossRef](#)]
32. Burke, M.; Blake, A.; Povey, I.M.; Schmidt, M.; Petkov, N.; Carolan, P.; Quinn, A.J. Low sheet resistance titanium nitride films by low-temperature plasma-enhanced atomic layer deposition using design of experiments methodology. *J. Vac. Sci. Technol. A* **2014**, *32*, 031506. [[CrossRef](#)]
33. Takeuchi, K.J.; Thompson, M.S.; Pipes, D.W.; Meyer, T.J. Redox and spectral properties of monooxo polypyridyl complexes of ruthenium and osmium in aqueous media. *Inorg. Chem.* **1984**, *23*, 1845–1851. [[CrossRef](#)]
34. Bucci, A.; Savini, A.; Rocchigiani, L.; Zuccaccia, C.; Rizzato, S.; Albinati, A.; Llobet, A.; MacChioni, A. Organometallic iridium catalysts based on pyridinecarboxylate ligands for the oxidative splitting of water. *Organometallics* **2012**, *31*, 8071–8074. [[CrossRef](#)]
35. Bignozzi, C.A.; Argazzi, R.; Scandola, F.; Schoonover, J.R.; Gordon, K.C.; Dyer, R.B. Electronic Coupling in Cyano-Bridged Ruthenium Polypyridine Complexes and Role of Electronic Effects on Cyanide Stretching Frequencies. *Inorg. Chem.* **1992**, *31*, 5260–5267. [[CrossRef](#)]
36. Ali, N.M.; Ward, M.D.; Hashim, N.; Daud, N. Synthesis and photophysical properties of bis(phenylpyridine) iridium(III) dicyanide complexes. *Mater. Res. Innov.* **2017**, 1–6. [[CrossRef](#)]
37. Wrzolek, P.; Schwalbe, M. Affecting the Catalytic Activity of the Known [Ru(tpy)(bpy)(OH₂)]²⁺ Complex in Water Oxidation by Utilization of a Hangman Ligand. *Eur. J. Inorg. Chem.* **2015**, 2015, 4373–4378. [[CrossRef](#)]
38. Cargill Thompson, A.M.W. The synthesis of 2,2':6',2''-terpyridine ligands—Versatile building blocks for supramolecular chemistry. *Coord. Chem. Rev.* **1997**, *160*, 1–52. [[CrossRef](#)]
39. Zuccaccia, C.; Bellachioma, G.; Bortolini, O.; Bucci, A.; Savini, A.; Macchioni, A. Transformation of a Cp*-iridium(III) precatalyst for water oxidation when exposed to oxidative stress. *Chem. Eur. J.* **2014**, *20*, 3446–3456. [[CrossRef](#)] [[PubMed](#)]
40. Wang, C.; Wang, J.L.; Lin, W. Elucidating molecular iridium water oxidation catalysts using metal-organic frameworks: A comprehensive structural, catalytic, spectroscopic, and kinetic study. *J. Am. Chem. Soc.* **2012**, *134*, 19895–19908. [[CrossRef](#)] [[PubMed](#)]
41. Hintermair, U.; Sheehan, S.W.; Parent, A.R.; Ess, D.H.; Richens, D.T.; Vaccaro, P.H.; Brudvig, G.W.; Crabtree, R.H. Precursor transformation during molecular oxidation catalysis with organometallic iridium complexes. *J. Am. Chem. Soc.* **2013**, *135*, 10837–10851. [[CrossRef](#)] [[PubMed](#)]
42. Park-Gehrke, L.S.; Freudenthal, J.; Kaminsky, W.; DiPasquale, A.G.; Mayer, J.M. Synthesis and oxidation of Cp*Ir(III) compounds: functionalization of a Cp* methyl group. *Dalt. Trans.* **2009**, 0, 1972. [[CrossRef](#)] [[PubMed](#)]
43. Thomsen, J.M.; Sheehan, S.W.; Hashmi, S.M.; Campos, J.; Hintermair, U.; Crabtree, R.H.; Brudvig, G.W. Electrochemical activation of Cp* iridium complexes for electrode-driven water-oxidation catalysis. *J. Am. Chem. Soc.* **2014**, *136*, 13826–13834. [[CrossRef](#)] [[PubMed](#)]

44. Goodall, W.; Wild, K.; Arm, K.J.; Williams, J.A.G. The synthesis of 4'-aryl substituted terpyridines by Suzuki cross-coupling reactions: substituent effects on ligand fluorescence. *J. Chem. Soc. Perkin Trans. 2* **2002**, 1669–1681. [[CrossRef](#)]
45. Xi, Y.; Wei, W.; Xu, Y.; Huang, X.; Zhang, F.; Hu, C. Coordination Polymers Based on Substituted Terpyridine Ligands: Synthesis, Structural Diversity, and Highly Efficient and Selective Catalytic Oxidation of Benzylic C–H Bonds. *Cryst. Growth Des.* **2015**, *15*, 2695–2702. [[CrossRef](#)]



© 2018 by the authors. Licensee MDPI, Basel, Switzerland. This article is an open access article distributed under the terms and conditions of the Creative Commons Attribution (CC BY) license (<http://creativecommons.org/licenses/by/4.0/>).